Transport with Reversed Shear in the National Spherical Torus Experiment

F. M. Levinton[1], H. Yuh[1], M. G. Bell[2], R. E. Bell[2], L. Delgado-Aparicio[3], M. Finkenthal[3], E. D. Fredrickson[2], D. A. Gates[2], S. M. Kaye[2], B. P. LeBlanc[2], R. Maingi[4], J. E. Menard[2], D. Mikkelsen[2], D. Mueller[2], R. Raman[5], G. Rewoldt[2], S. A. Sabbagh[6], D. Stutman[3], and K. Tritz[3], W. Wang[2]

[1]Nova Photonics, Inc., Princeton, NJ 08540

[2]Princeton Plasma Physics Laboratory, Princeton, NJ 08543

[3]Johns Hopkins University, Baltimore, MD 21218

[4]Oak Ridge National Laboratory, Oak Ridge, TN 37830

[5]University of Washington, Seattle, WA 98195

[6]Columbia University, New York, NY 10027

In the National Spherical Torus Experiment (NSTX), plasmas with strongly reversed magnetic shear $(r/q)(dq/dr < 0)$ in the plasma core exhibit a marked improvement in electron confinement compared to otherwise similar plasmas with positive or only weakly reversed magnetic shear. The q-profile is determined by the early evolution of the plasma current, the plasma cross-section, and the neutral-beam heating power. In the region of shear reversal, the electron thermal diffusivity can be significantly reduced. Detailed experimental investigation of this phenomenon has been made possible by the successful development of a motional Stark effect (MSE) polarimetry diagnostic suitable for the low magnetic field in NSTX, typically 0.35 – 0.55 T. Several of the unique features of this system will be highlighted. Measurements of the electron and ion temperature, density, and plasma toroidal rotation profiles are also available with high spatial and temporal resolution.

I Introduction

The economic attractiveness of fusion energy could be greatly enhanced by improved transport and stability in fusion devices. Fusion experiments frequently find cross-field transport to be anomalously high compared to predictions of neoclassical theory, which attributes the energy and particle transport to Coulomb collisions. Several experiments have found regimes of transport with improved confinement such that the magnetic shear, $s = (r/q)dq/dr < 0$. These reversed shear regimes typically have improved confinement of the ions and frequently, but not always, improvement of the electron thermal diffusivity [1–5]. An understanding of the physics involved in the ion transport reduction has begun to emerge. Several theoretical studies have found that a reduction of the interchange drive due to reversed shear can help stabilize or reduce the growth rate of ion temperature gradient (ITG) and trapped electron mode (TEM) micro instabilities [6–8]. Even without completely stabilizing the mode, increased $E_r \times B$ flow shear causes decorrelation of the turbulence resulting in a reduction of thermal transport [9, 10]. Several experimental results and supporting theoretical models have supported this paradigm [11–15]. Despite the complexity of all the effects including magnetic shear, ion to electron temperature ratio, Shafranov shift, and velocity shear, the computational models have made good progress at predicting stabilization of ITG and TEM instabilities.

Development of an understanding of the electron thermal transport still remains a challenge and continues to be a very active subject of ongoing research, both experimentally and theoretically. An understanding of electron heating and transport is very important because the main heating mechanism in reactor plasmas will be by the α-particles which transfer their heat mainly to the electrons. One reason for the difficulty of developing a theoretical understanding of the electron channel is the non-linear nature and small scale of the electron gyro-scale instabilities and the large range of scale lengths needed to solve this problem.

Several experiments using predominantly electron heating have observed regimes of improved electron confinement [16–26]. In these experiments it is believed that reversed shear is playing an important role leading to improved electron confinement. However, local magnetic measurements from MSE are lacking in most cases to provide definitive data of the q-profile evolution. In neutral beam heated plasmas, the electron thermal diffusivity is often not changed with reversed shear [1, 2]. In some cases where it has improved during neutral beam heating, it was affected only over a narrow spatial region near the q_{min} radius [27–29]. One hypothesis is that the electron temperature gradient (ETG) mode is responsible for the high electron transport routinely observed. The mode has a short wavelength and can exist without affecting the ion transport as has been observed in some measurements in which $\chi_i \ll \chi_e$.

In this paper we report on transport measurements in the low aspect ratio National Spherical Torus Experiment (NSTX). The electron and ion transport, in beam heated discharges, show a clear reduction of the electron thermal diffusivity with reversed shear q-profiles and in some cases both the electron and ion thermal diffusivites are reduced.

In section II the motional Stark effect collisional induced fluorescence (MSE-CIF) polarimetry diagnostic is briefly described, as it has several unique features due to the low magnetic field of NSTX. The equilibrium reconstruction using the MSE-CIF data is discussed. Section III has a discussion of the formation and evolution of the reversed shear discharge including a case which transitions from reversed shear to one having a flat q-profile (low central shear) in the plasma core due to an MHD reconnection event. In section IV the transport analysis and results will be described and conclusions are in section V.

II Diagnostics

The NSTX experiment is a low-aspect-ratio spherical torus [30, 31]. The plasmas used in this study are L-mode type with about 2 MW of neutral beam heating. An extensive set of diagnostics are used for transport analysis including ion temperature, ion density, Z-effective, and toroidal flow from the CHERS diagnostic, electron temperature and density from Thomson scattering, and q-profile from the MSE-CIF polarimetry diagnostic. The MHD diagnostics include the Mirnov coils and soft x-ray array. The measurements of the q-profile are made with the motional Stark effect polarimetry diagnostic [32]. The NSTX experiment operates at a toroidal magnetic field of 0.35-0.55 T. This is a significantly lower toroidal magnetic field than any previous implementation of MSE-CIF polarimetry has measured. In order to obtain a strongly polarized emission signal from the Stark multiplet a narrow band filter is usually employed to separate out a portion of the spectrum. The spectral splitting of the Stark multiplet is linearly proportional to the magnetic field, so for the low magnetic field of NSTX the filter bandwidth needed to be reduced substantially. In order to implement the MSE-CIF diagnostic on NSTX, development was required of a new optical filter to achieve higher resolution and throughput than was possible with a conventional interference filter. The filter is based on a wide field Lyot birefringence interference filter. The spectral resolution of the filter is 0.062 nm with each channel having 76 fibers that are 1 mm in diameter imaged through it. Shown in Fig. 1 is the measured spectrum from NSTX of Doppler shifted H_α emission from the heating beam. For comparison is the calculated Stark multiplet and its convolution compared to the measured spectrum. A conventional interference filter with a bandpass of 0.3-0.4 nm would integrate over the entire Stark multiplet of π and σ transitions resulting in a very low polarization fraction, estimated to be $\sim 2\%$. The narrow band Lyot filter can isolate a portion of the spectrum, such as the π lines, to yield a much higher polarization fraction, measured to be 40%. With the good polarization fraction using the Lyot filter and large

étendue, the resulting time resolution is 5-10 ms with a statistical uncertainty of $\sim 0.3^{\circ}$ for the measured magnetic field pitch angle. A plan view of the MSE-CIF diagnostic on NSTX is shown in Fig. 2. The diagnostic uses one of the neutral beam sources. The MSE-CIF system presently has 12 sightlines operating out of a possible 19, covering from the magnetic axis to the outboard edge, with a spatial resolution of 2-3 cm.

The magnetic field pitch angle from the MSE-CIF diagnostic, along with the external coil currents, magnetic field coils, and flux loop measurements are input into the free boundary LRDFIT equilibrium reconstruction code. LRDFIT includes a circuit model of the vacuum vessel that has been validated by experiments. It includes a T_e iso-surface constraint and toroidal rotation effects. The MSE-CIF data is corrected for the radial electric field, E_r, due to toroidal rotation and pressure gradients terms in the radial force balance shown in Eq.(1) using the CHERS data. E_r is given by the radial force balance equation,

$$E_r = \frac{1}{n_i Z_i e} \nabla P_i - v_{\theta i} B_{\phi} + v_{\phi i} B_{\theta} \tag{1}$$

where P_i is the ion pressure, n_i is the ion number density, $Z_i e$ is the ion charge, $v_{\theta i}(v_{\phi i})$ is the poloidal(toroidal) velocity, and $B_{\theta}(B_{\phi})$ is the poloidal (toroidal) magnetic field. The E_r correction does not yet include effects from poloidal flow, which are expected to only affect the data at the edge. Shown in Fig. 3 is a reconstruction from LRDFIT of two cases of the pitch angle profile compared to the input MSE-CIF data. The MSE-CIF error bars are shown in the plot by the size of the symbol. The reconstruction from LRDFIT has low residuals of $\sim 0.3^{\circ}$ in the plasma core, consistent with the MSE-CIF statistical uncertainties. The bands on the reconstructed q-profiles from LRDFIT represent the variation of the q-profile by varying the input parameters to LRDFIT.

III q-profile Development and Evolution

We have several controls to vary the startup and evolution of the current density profile. Such variables as the plasma growth and shape, plasma current ramp rate, neutral beam timing, and gas fueling all have a strong effect on the current profile evolution. The basic reversed shear development scenario is to have a large plasma as early as possible during the current ramp up phase. In this way the current will penetrate from the edge forming a hollow current profile. The large size of the plasma will mean it takes longer for the current to reach the core. In order to slow the current penetration to the plasma core and maintain the hollow current profile, early neutral beam heating is applied. We have found that without careful control of the various parameters such as the current ramp rate and neutral beam timing, MHD can occur that causes reconnection and a very rapid current redistribution. However, with the MSE-CIF diagnostic to monitor the effects of MHD, the development can be optimized to produce the desired results. Fig. 4 shows the waveforms for the current ramp-up, neutral beam timing, and the peak electron temperature for two cases. The two cases have the same growth and current ramp up, but different timing for the start of neutral beam injection. The latter start time is our reversed shear scenario. Shown in Fig. 5 is the $q(0)$, q_{min}, MHD evolution, and q-profiles for this case. The neutral beam is turned on at 0.2 s, just before $q(0)$ and q_{min} cross 2. They decrease as the current slowly penetrates to the plasma center. As q_{min} approaches 1, the MHD begins to grow until q_{min} reaches 1, at which time the mode locks and the plasma collapses. Prior to that the MHD is very quiescent.

The case with the earlier start of neutral beam injection begins with a high q(0) that is strongly reversed, but undergoes an MHD triggered reconnection that flattens the q-profile producing a substantial region of low magnetic shear. The time evolution of $q(0)$ and q_{min} and the MHD from the Mirnov coil is shown in Fig. 6. Prior to a small MHD event at 0.235 s

q(0) is 3.5. The next time slice has $q(0)$ at about 2, with little change in q_{min}. The MSE-CIF q-profiles, in Fig. 6, show a large difference before and after the MHD reconnection occurs. After the reconnection event the q-profile is flat inside of $q = 2$. Large changes such as this are not predicted by any model and emphasize the need for local measurements of the magnetic field pitch angle profile to correctly determine the current density evolution. The parallel current density profile, shown in Fig. 7, is calculated from the LRDFIT equilibrium reconstruction code. It is interesting to compare this to the soft x-ray array diagnostic, shown in Fig. 8. The x-ray data has been mapped, using the equilibrium from LRDFIT to the minor radius. The radii of the x-ray chords corresponds to the location of the peak calculated emission, based on mapping the electron density, electron temperature, and Z-effective to the flux surfaces and calculating the local intensity. The x-ray data shows a sawtooth like event that occurs at 0.235 seconds. The location where the parallel current density profiles cross, near ($r/a \sim 0.25$), corresponds closely to the inversion radius of the x-ray data. Also, the outboard edge of the x-ray data extends to the location of the q_{min} radius, that is shown in Fig. 7

IV Transport Analysis

The local transport analysis is done using the TRANSP code [33] with all the available kinetic profile data and equilibrium from the LRDFIT reconstruction with MSE-CIF. To evaluate the effect of the q-profile and in particular the local magnetic shear, on the transport, we shall compare two cases. (i) Two different discharges, one that remained with a reversed shear q-profile and another that did not. (ii) A discharge that transitions from a reversed shear q-profile to a low central shear q-profile. In case (i) the peak electron temperature, Mirnov coil data, and $q(0) - q_{min}$ evolution are shown in Fig. 9 and the q-profiles and electron temperature profiles in Fig. 10. Neither discharge has any appreciable MHD

at the time of interest or for some duration before. The reversed shear discharge has a much more peaked electron temperature profile shown in Fig. 10. The location at which the two temperature profiles begin to strongly diverge, at 1.25 m, corresponds to the q_{min} radius. Outboard of the q_{min} radius the temperature profiles are very similar. This is also much the same for the density profiles. The ion temperature profile shows a similar behavior for the two cases, as shown in Fig. 11, however the toroidal velocity profiles show little difference. The corresponding electron and ion thermal diffusivities for these two discharges are shown in Fig. 12. The reversed discharge has a lower electron thermal diffusivity by almost an order of magnitude compared to the discharge with low central shear. They diverge strongly inside of $r/a \sim 0.4$, which corresponds to the region of the reversed the shear as shown in Fig. 13. The ion transport also shows some improvement in the plasma core, however the estimated neoclassical value as calculated by NCLASS [34] also decreases. This is consistent with the ion thermal diffusivity remaining near the neoclassical level in the plasma core.

As described earlier, a discharge makes a transition from reversed shear to low central shear over a very short time interval. The evolution of $q(0)$, q_{min}, MHD, and the q-profie change are shown in Fig. 6 and Fig. 7. The electron thermal diffusivity also increases just after the reversed shear profile changes to low central shear, shown in Fig. 14. Like the previous case the change in χ_e is almost an order of magnitude and the sharp change in the χ_e profiles occurs inboard of the q_{min} radius. Unlike the previous case the χ_i profiles do not change significantly, as shown in Fig. 14, but nor does the neoclassical level. In this case also both the reversed shear and low central shear χ_i profiles are near or slightly above the calculated neoclassical level in the plasma core.

V Conclusions

The goal of this experiment was to generate various q-profiles with differing shear, as determined by detailed measurements with the MSE-CIF diagnostic. Several cases were well documented from reversed shear to monotonic q-profiles. The correlation between reversed magnetic shear and improved electron thermal diffusivity in NSTX is clearly shown and that weak shear is not sufficient. This would rule out the zero-shear gap (ZSG) model [35]. This theory attempts to explain the reduction of transport by an increase in the distance between resonant surfaces in the region of low shear. If this were the case one would expect the flat q-profile in Fig. 6 to have the better transport, but in fact it does not. Our results are also not consistent with models that depend on rational q-surfaces and are independent of shear [25]. We also see the improvement in χ_e over the entire region from the q_{min} radius to the magnetic axis. Several experimental results observe the improvement only over a narrow region at the q_{min} radius. The regime we are operating in on NSTX has the ion thermal transport at or near neoclassical levels. This is consistent with calculations of ITG/TEM microinstabilities which indicate that with flow shear they are fully stabilized in the plasma core. A natural candidate for the electron transport would be the shorter wavelength electron temperature gradient (ETG) turbulence [36]. Nonlinear numerical simulations of of ETG turbulence show a reduction of electron transport is possible with reversed shear and high beta [37]. Linear gyrokinetic microstability calculations for similar plasmas in NSTX [38] were performed with the GS2 code [39]. For those cases the reversed shear q-profile was found to be more stable to ETG than the low shear q-profile. Detailed analysis of these cases with both linear and non-linear gyrokinetic calculations will be done in the future.

Acknowledgments

This research is supported by US DOE grant DE-FG02-99ER54520 and US DOE contract DE-AC02-76CHO3073.

References

[1] F. M. Levinton et al., Phys. Rev. Lett. **75**, 4417 (1995).

[2] E. J. Strait et al., Phys. Rev. Lett. **75**, 4421 (1995).

[3] O. Gruber et al., Phys. Rev. Lett **83**, 1787 (1999).

[4] S. Ishida et al., Phys. Rev. Lett. **79**, 3917 (1997).

[5] C. Gormezano et al., Phys. Rev. Lett. **80**, 5544 (1998).

[6] J. F. Drake et al., Phys. Rev. Lett. **77**, 494 (1996).

[7] R. E. Waltz, G. D. Kerbel, J. Milovich, and G. W. Hammett, Phys. Plasmas **2**, 2408 (1995).

[8] M. A. Beer, G. W. Hammett, G. Rewoldt, E. J. Synakowski, and M. C. Zarnstorff, Phys. Plasmas **4**, 1792 (1997).

[9] F. L. Hinton and G. M. Staebler, Phys. Fluids B **5**, 1281 (1993).

[10] G. M. Staebler et al., Phys. Plasmas **1**, 909 (1994).

[11] K. H. Burrell, Phys. Plasmas **4**, 1499 (1997).

[12] E. J. Synakowski et al., Phys. Rev. Lett. **78**, 2972 (1997).

[13] C. Gormezano, Plasma Phys. Controlled Fusion **41**, B367 (1999).

[14] Y. Kamada, Plasma Phys. Controlled Fusion **42**, A65 (2000).

[15] P. W. Terry, Rev. Mod. Phys. **72**, 109 (2000).

[16] X. Litaudon et al., Plasma Phys. Control. Fusion **43**, 677 (2001).

[17] E. Barbato, Plasma Physics and Controlled Fusion **43**, A287 (2001).

[18] P. Buratti et al., Phys. Rev. Lett. **82**, 560 (1999).

[19] N. C. Hawkes et al., Plasma Phys. Controlled Fusion **44**, 1105 (2002).

[20] N. A. Kirneva et al., Plasma Phys. Controlled Fusion **47**, 1787 (2005).

[21] C. Gormezano et al., Plasma Phys. Controlled Fusion **46**, B435 (2004).

[22] Y. F. Baranov et al., Plasma Phys. Controlled Fusion **46**, 1181 (2004).

[23] T. Fujita et al., Plasma Phys. Controlled Fusion **46**, A35 (2004).

[24] K. A. Razumova et al., Nucl. Fusion **42**, 973 (2000).

[25] G. M. D. Hogeweij, N. J. L. Cardozo, M. R. D. Baar, and A. M. R. Schilham, Nucl. Fusion **38**, 1881 (1998).

[26] M. A. Henderson et al., Phys. Rev. Lett. **93**, 215001 (2004).

[27] B. W. Stallard et al., Phys. Plasmas **6**, 1978 (1999).

[28] T. Fujita et al., Phys. Rev. Lett. **78**, 2377 (1997).

[29] M. G. Bell et al., Plasma Phys. Controlled Fusion **41**, A719 (1999).

[30] M. Ono et al., Nucl. Fusion **40**, 557 (2000).

[31] S. M. Kaye et al., Nucl. Fusion **45**, S168 (2005).

[32] F. M. Levinton et al., Phys. Rev. Lett. **63**, 2060 (1989).

[33] R. J. Hawryluk, An empirical approach to tokamak transport, in *Proc. Course in Physics of Plasmas Close to Thermonuclear Conditions, Varenna 1979*, volume I, page 19, CEC, Brussels, 1980.

[34] W. Houlberg, K. C. Shaing, S. P. Hirshman, and M. C. Zarnstorff, Phys. Plasmas **4**, 3230 (1997).

[35] Y. Kishimoto et al., Nuc. Fusion **40**, 667 (2000).

[36] W. Horton, B. G. Hong, and W. M. Tang, Phys. Fluids **31**, 2971 (1988).

[37] F. Jenko, W. Dorland, M. Kotschenreuther, and B. N. Rogers, Phys. Plasmas **7**, 1904 (2000).

[38] D. Stutman et al., Phys. Plasmas **13**, 092511 (2006).

[39] M. Kotschenreuther, G. Rewoldt, and W. M. Tang, Comput. Phys. Commun. **88**, 128 (1995).

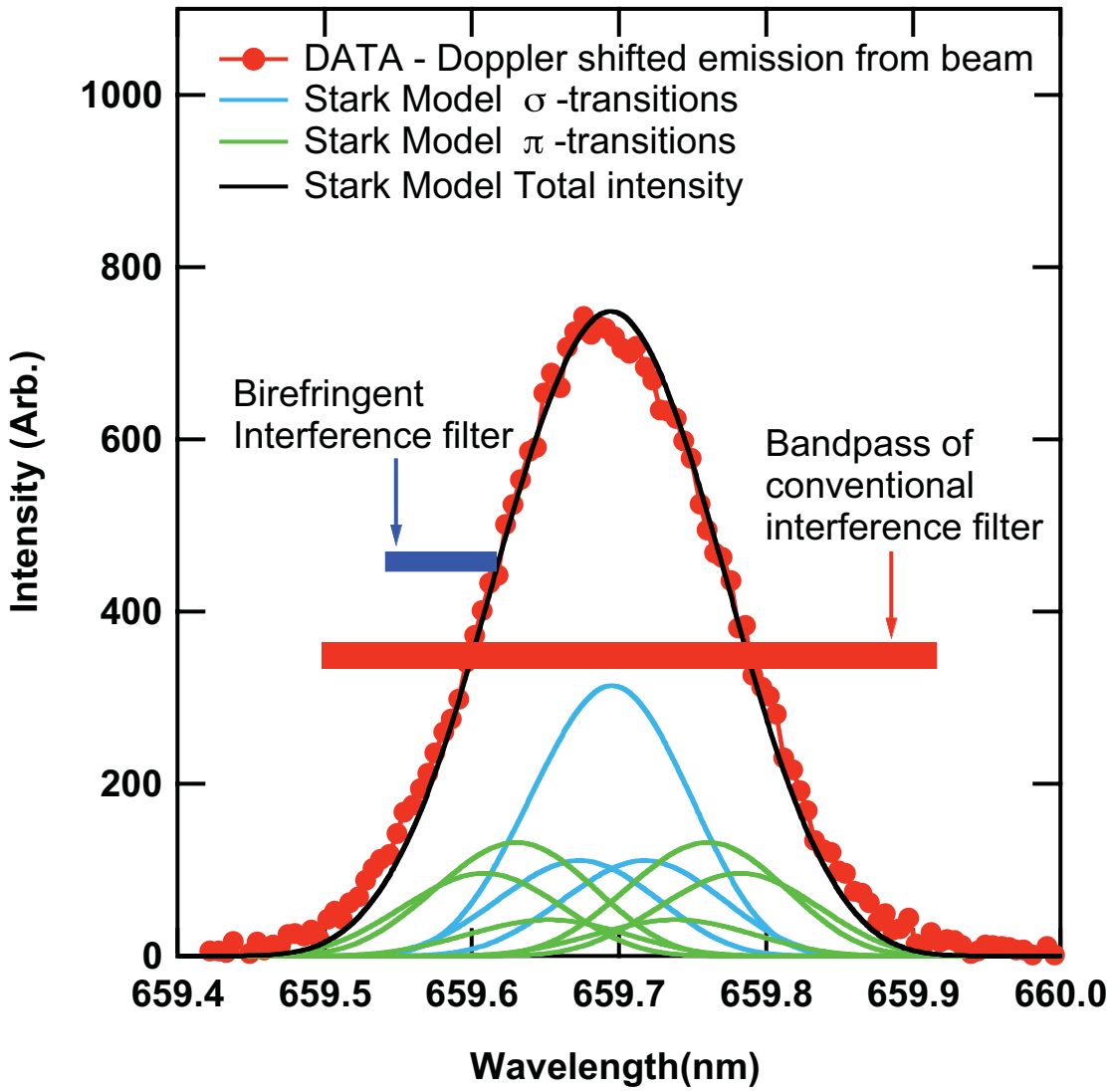

Figure 1: Measured spectrum from NSTX of Doppler shifter H_α emission from the heating beam. Comparison of the calculated Stark multiplet and its convolution is compared to the measured spectra.

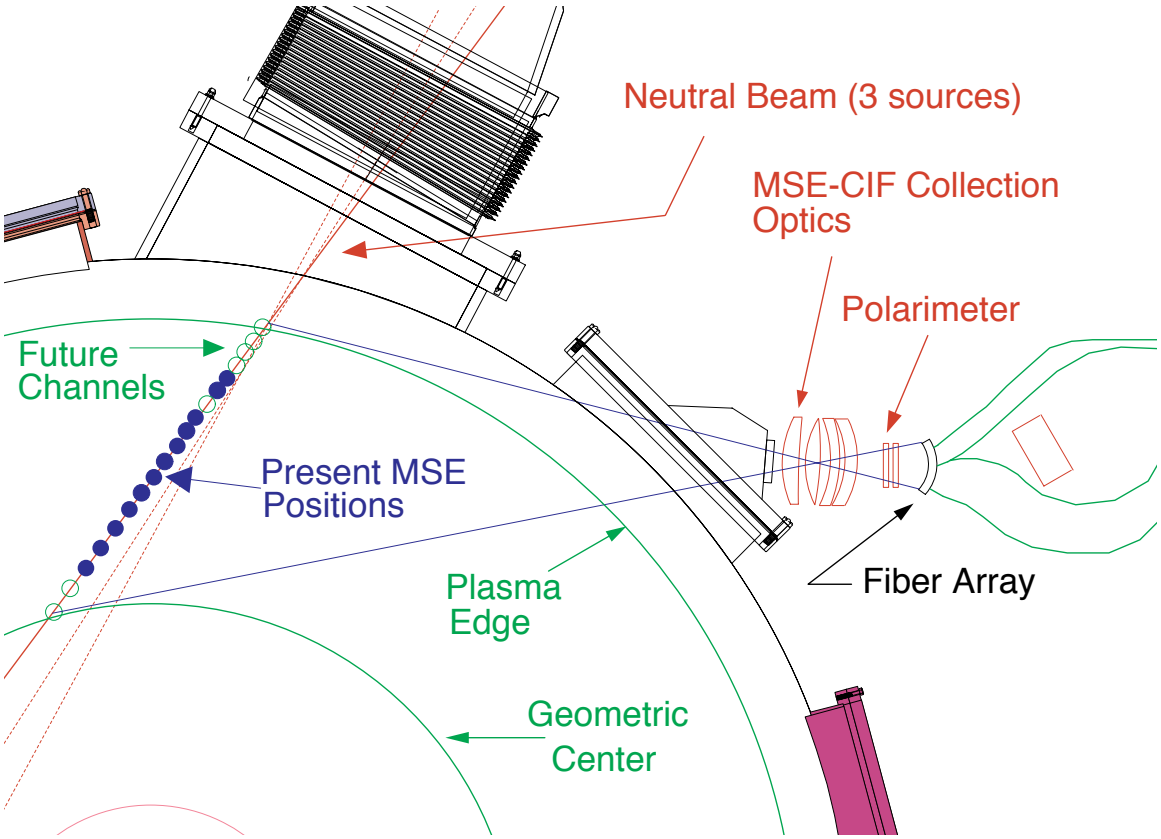

Figure 2: Plan view of MSE-CIF layout on NSTX.

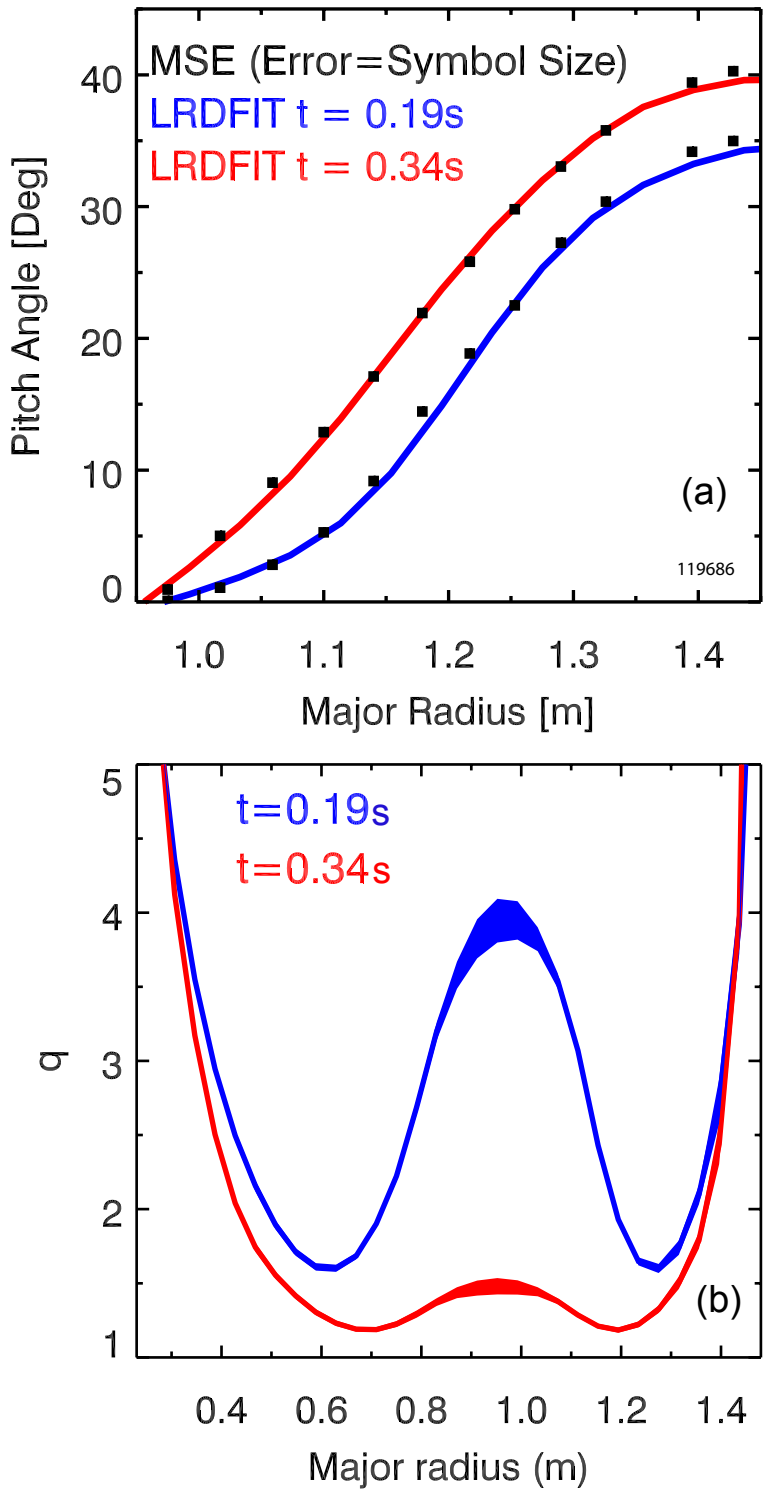

Figure 3: MSE-CIF data at two times and reconstruction results from LRDFIT of (a) the pitch angle and (b) the q-profile. The bands on the q-profile represents the variability from LRDFIT.

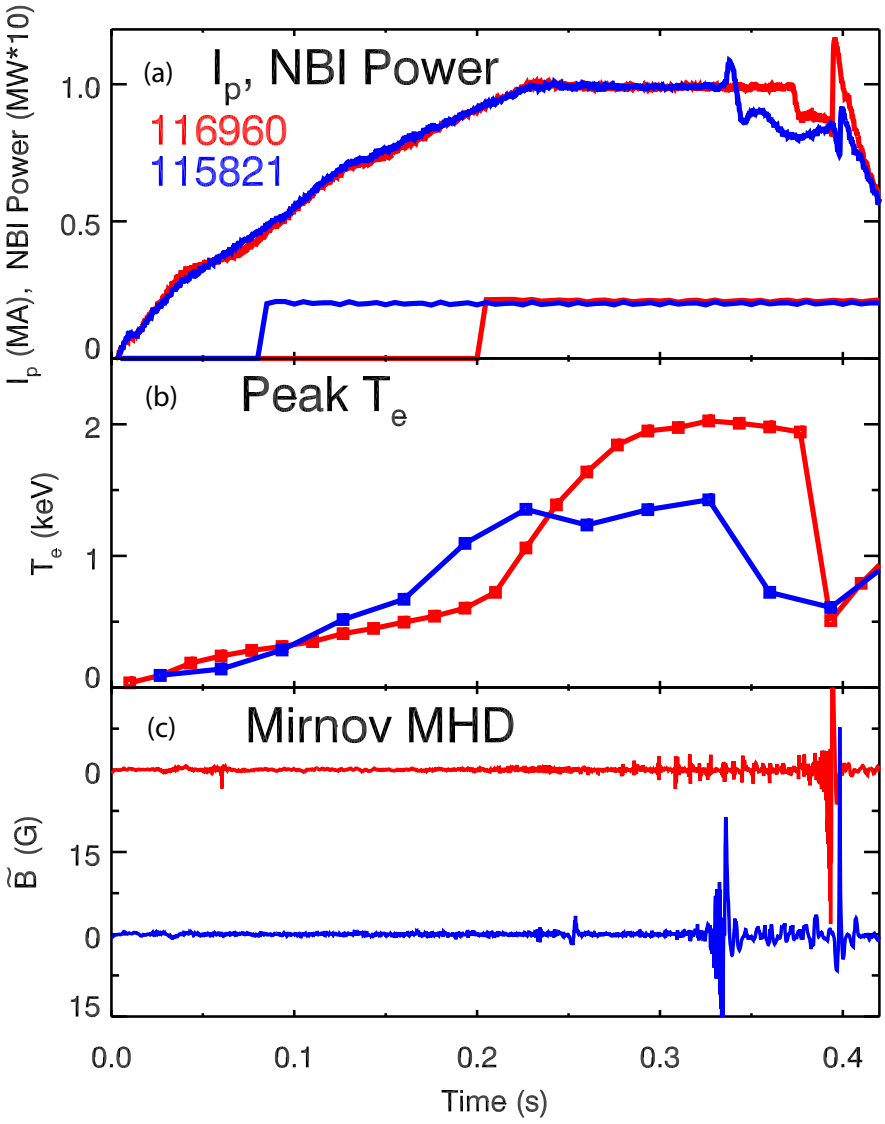

Figure 4: (a) The plasma current, neutral beam power, (b) peak electron temperature, and (c) Mirnov coil signals for two discharges. In red with a reversed shear q-profile and in blue with a low central shear q-profile.

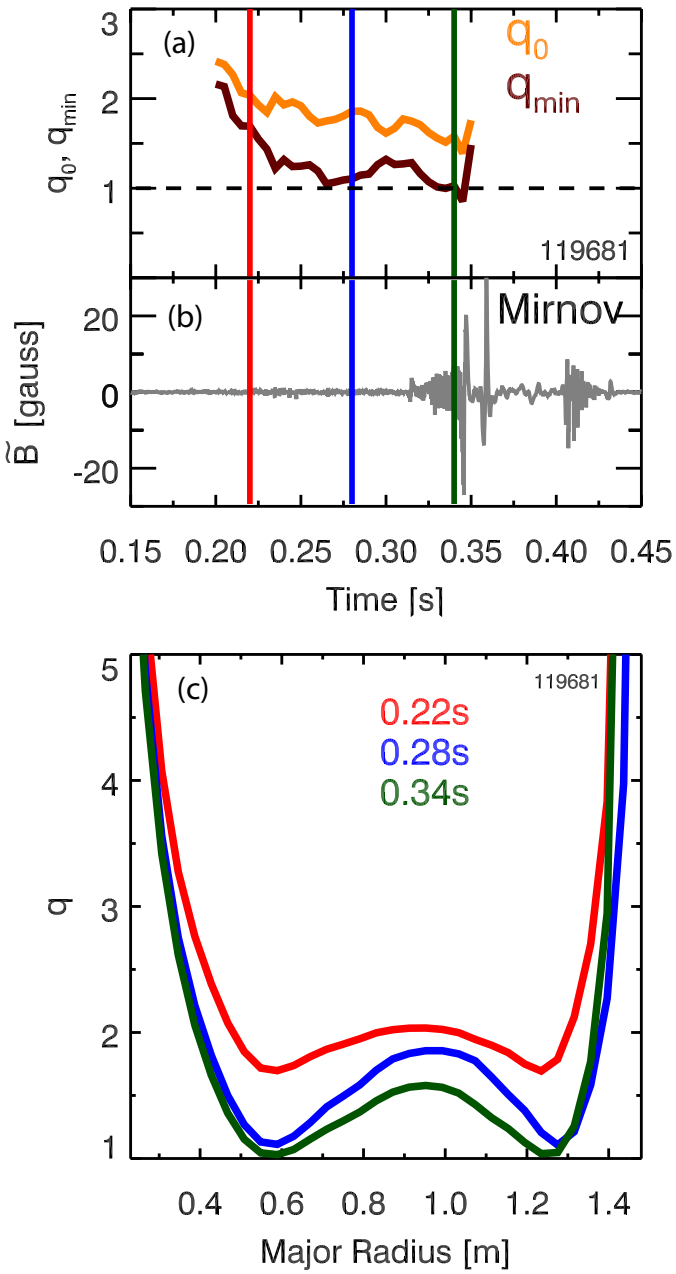

Figure 5: A typical reversed shear discharge evolution of (a) $q(0)$, q_{min}, and (b) Mirnov coil data. (c) The q-profiles correspond to times shown by vertical lines in plots above.

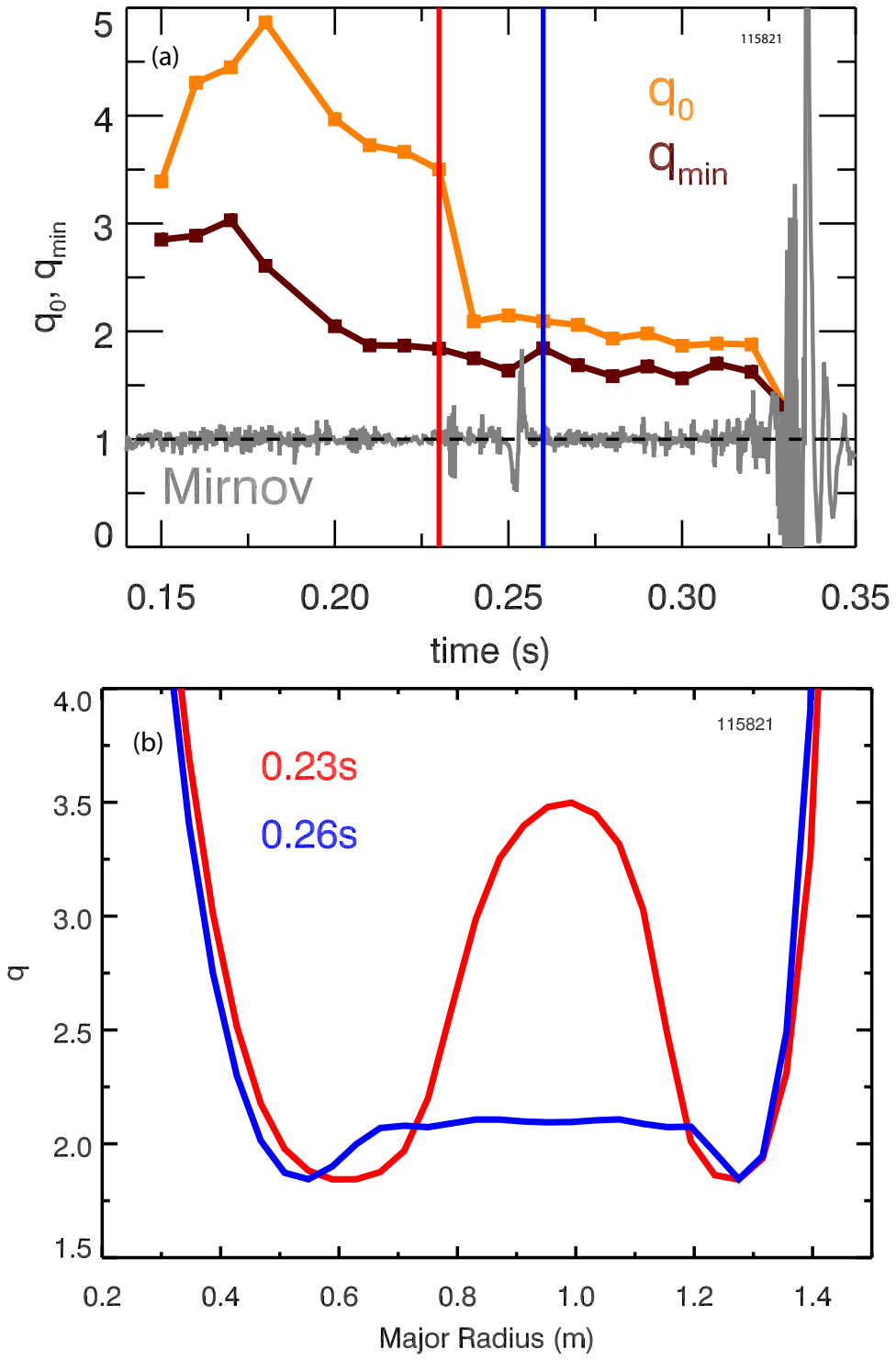

Figure 6: The (a) $q(0)$ and q_{min} evolution. At 0.235 seconds $q(0)$ drops precipitously following an MHD event. (b) The q-profiles just before and after the MHD event at 0.235 s.

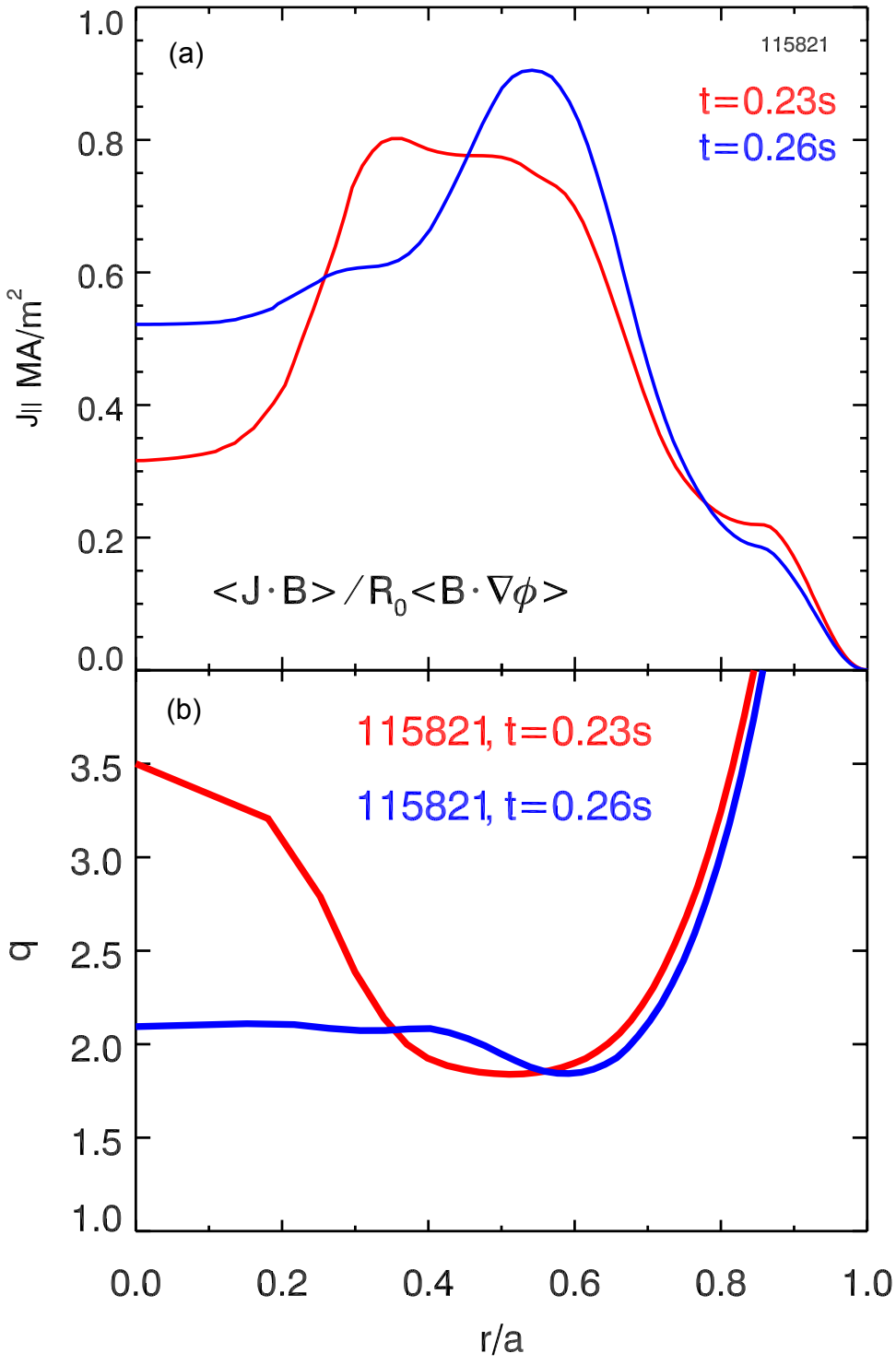

Figure 7: (a) Parallel current density profile and (b) $q(r/a)$ before and after reconnection.

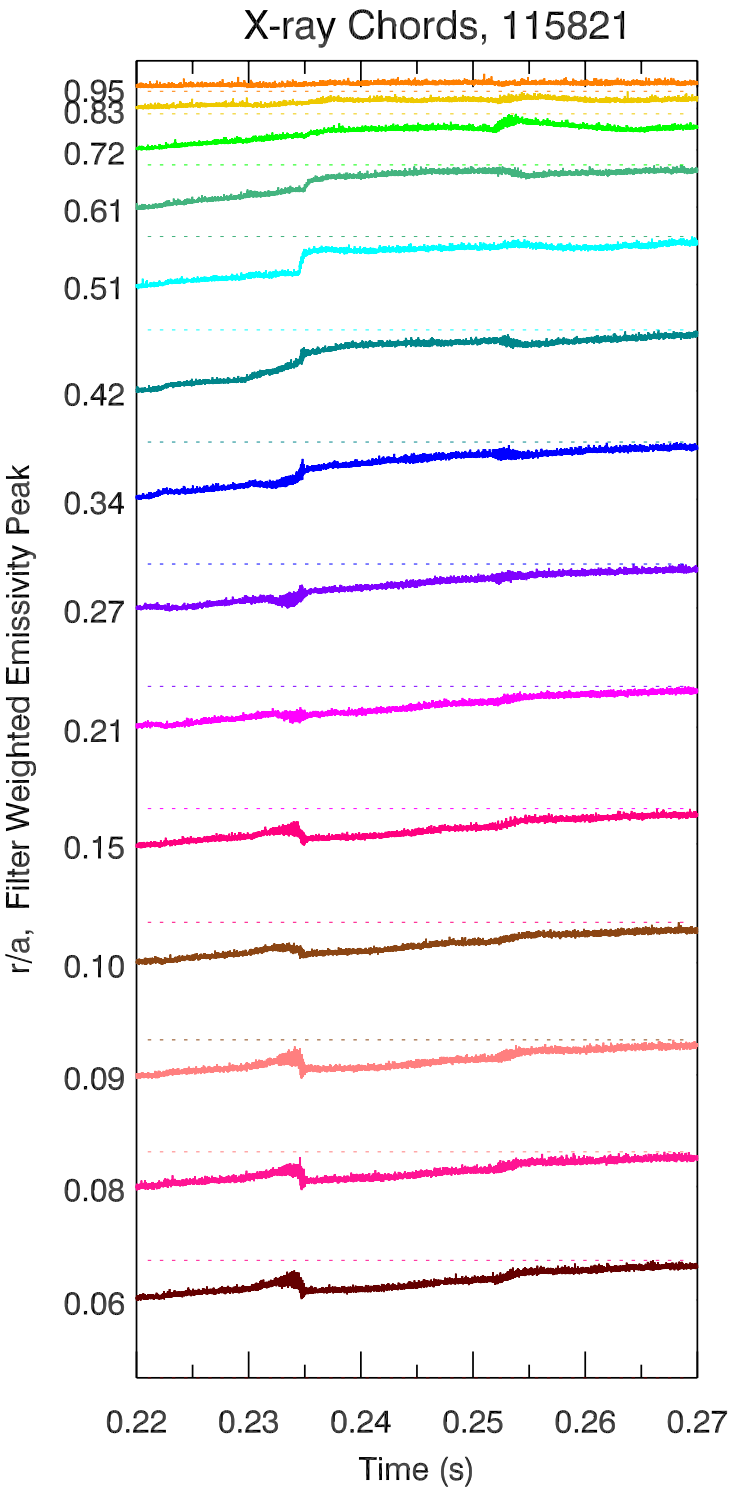

Figure 8: Soft X-ray data with sawtooth-like MHD event at 0.235 seconds.

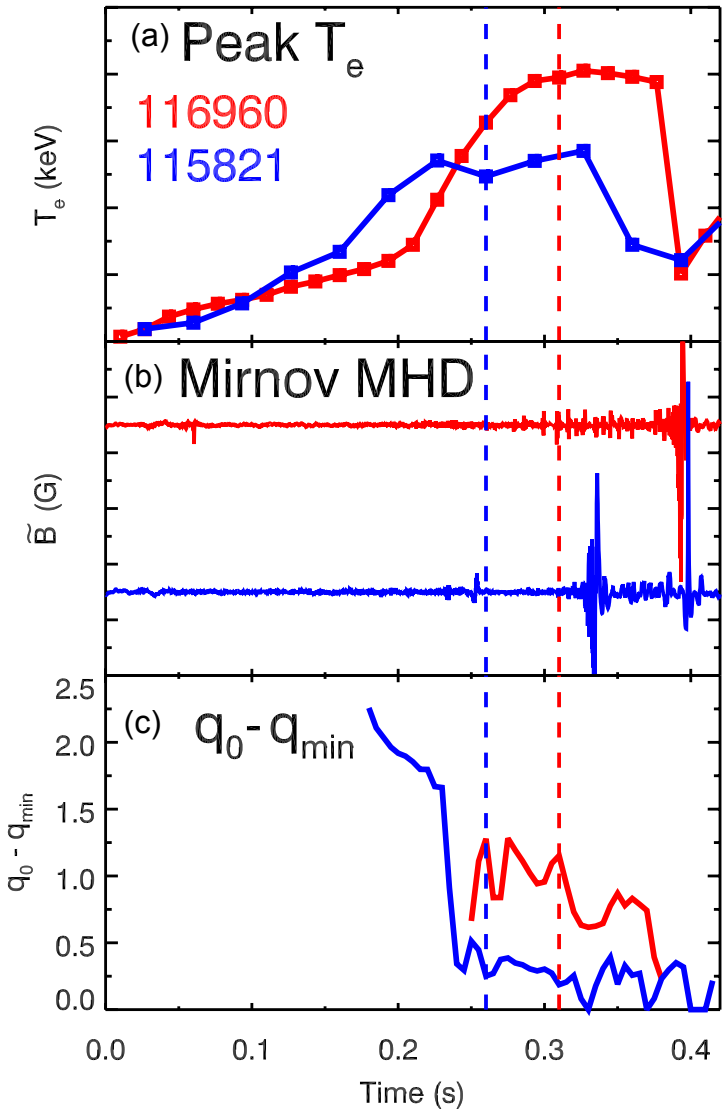

Figure 9: Comparison of (a) peak electron temperature evolution, (b) Mirnov coil data, and (c) $q(0) - q_{min}$ evolution for reversed shear (red) discharge and low shear discharge (blue).

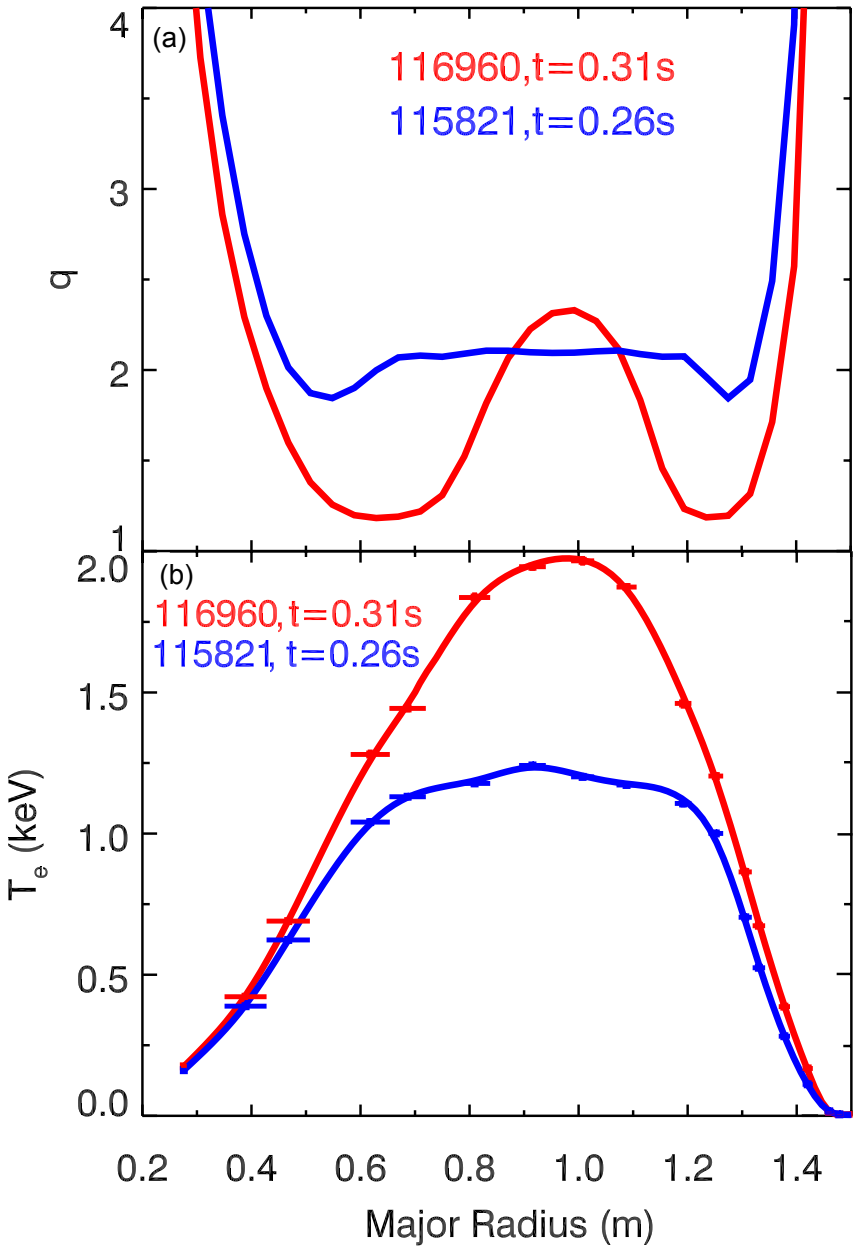

Figure 10: The (a) q-profiles and (b) electron temperature profiles at times shown in the previous figure with vertical lines.

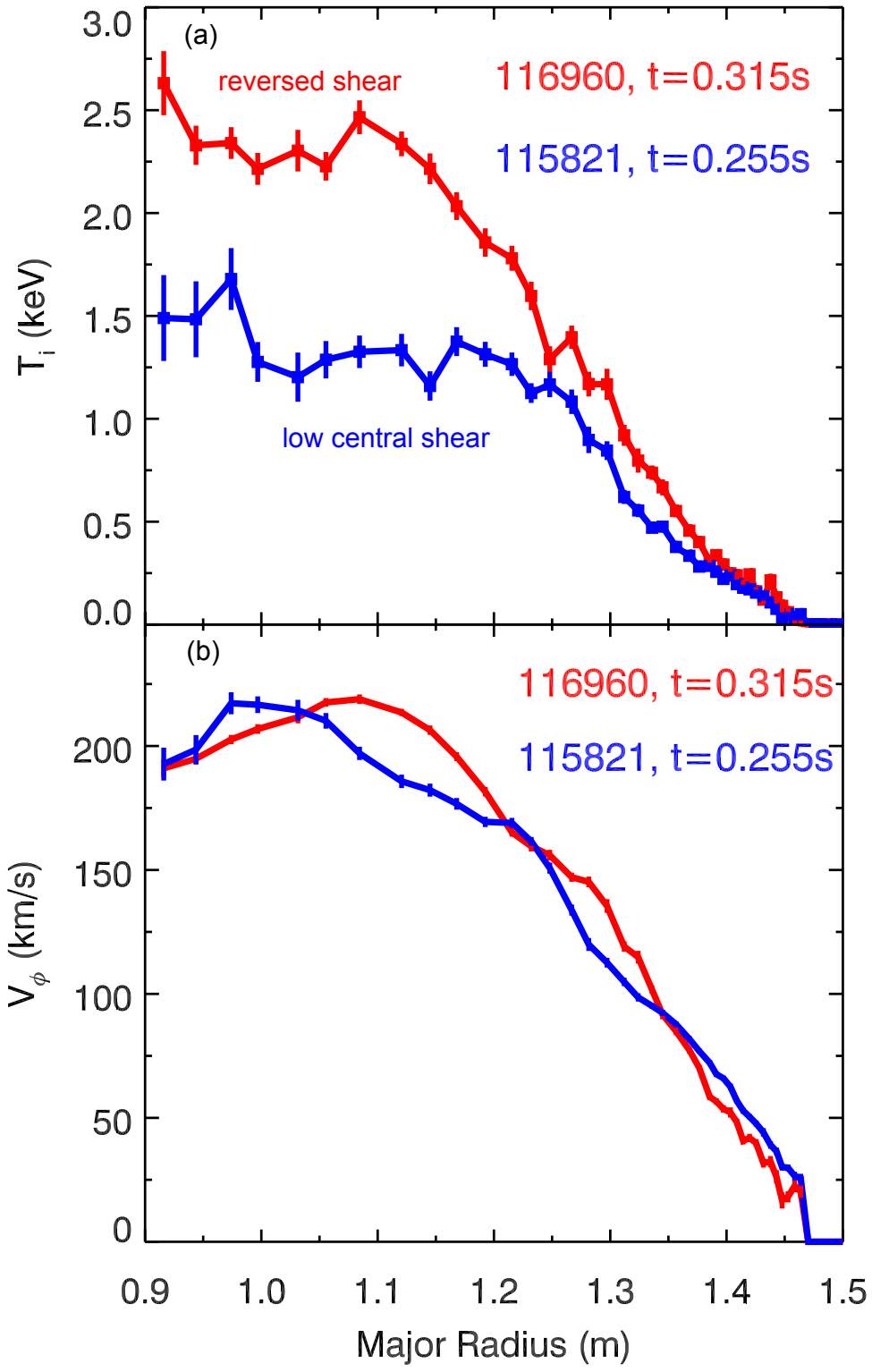

Figure 11: The (a) ion temperature and (b) toroidal rotation velocities at 0.315 s for the reversed shear discharge and 0.255 s for the low central shear discharge.

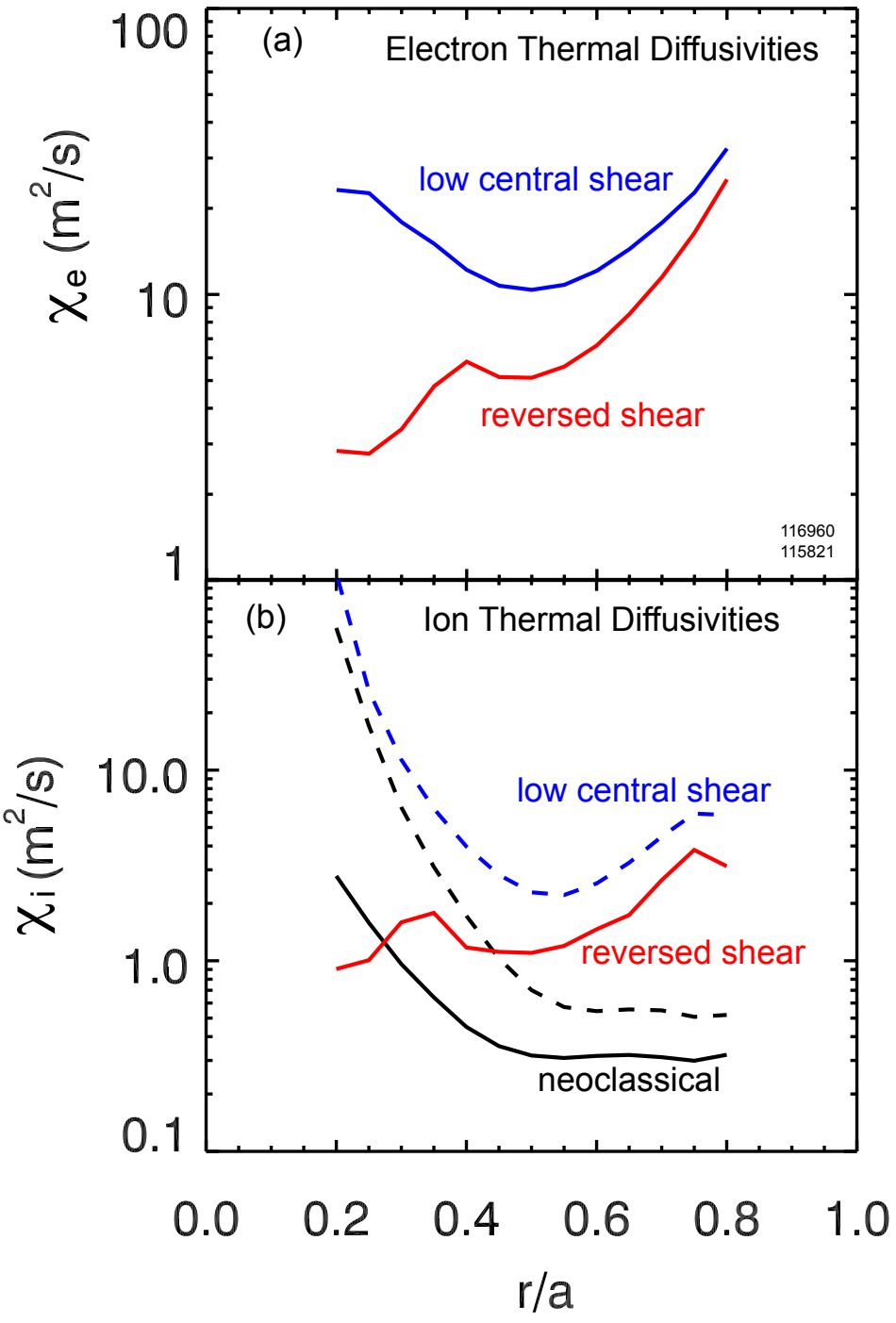

Figure 12: The (a) electron thermal diffusivity for the low central shear and reversed shear cases. (b) Comparison of ion thermal diffusivity of the reversed shear (solid red), low central shear (dashed blue) and neoclassical calculations for low central shear (dashed black) and reversed shear (solid black).

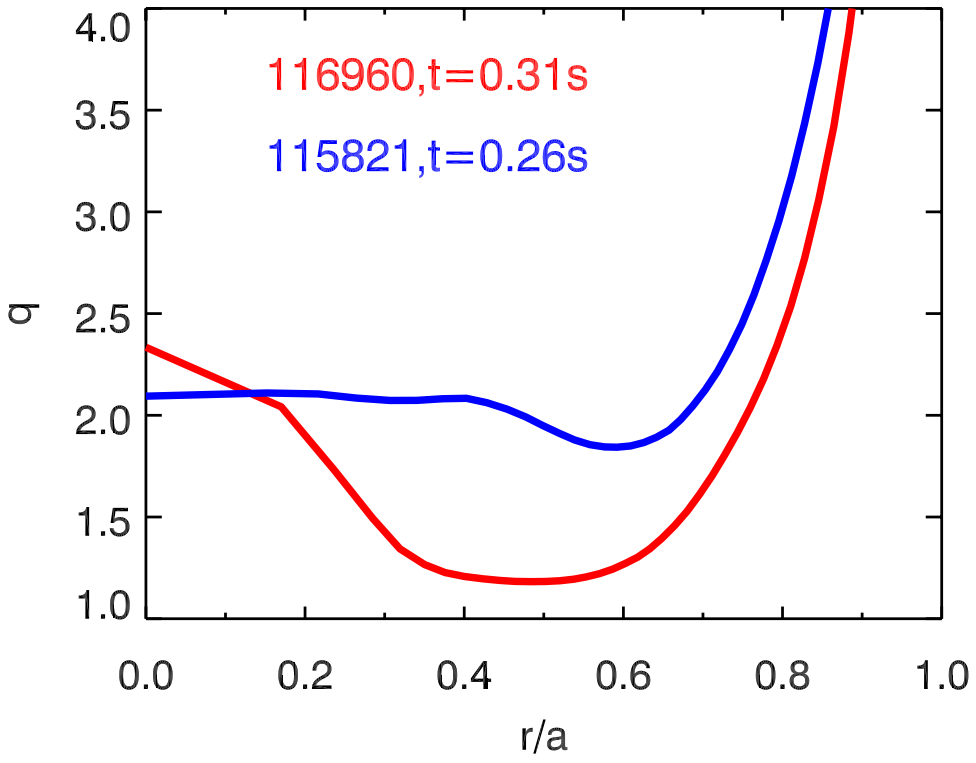

Figure 13: q(r/a) for the reversed shear and low central shear discharges.

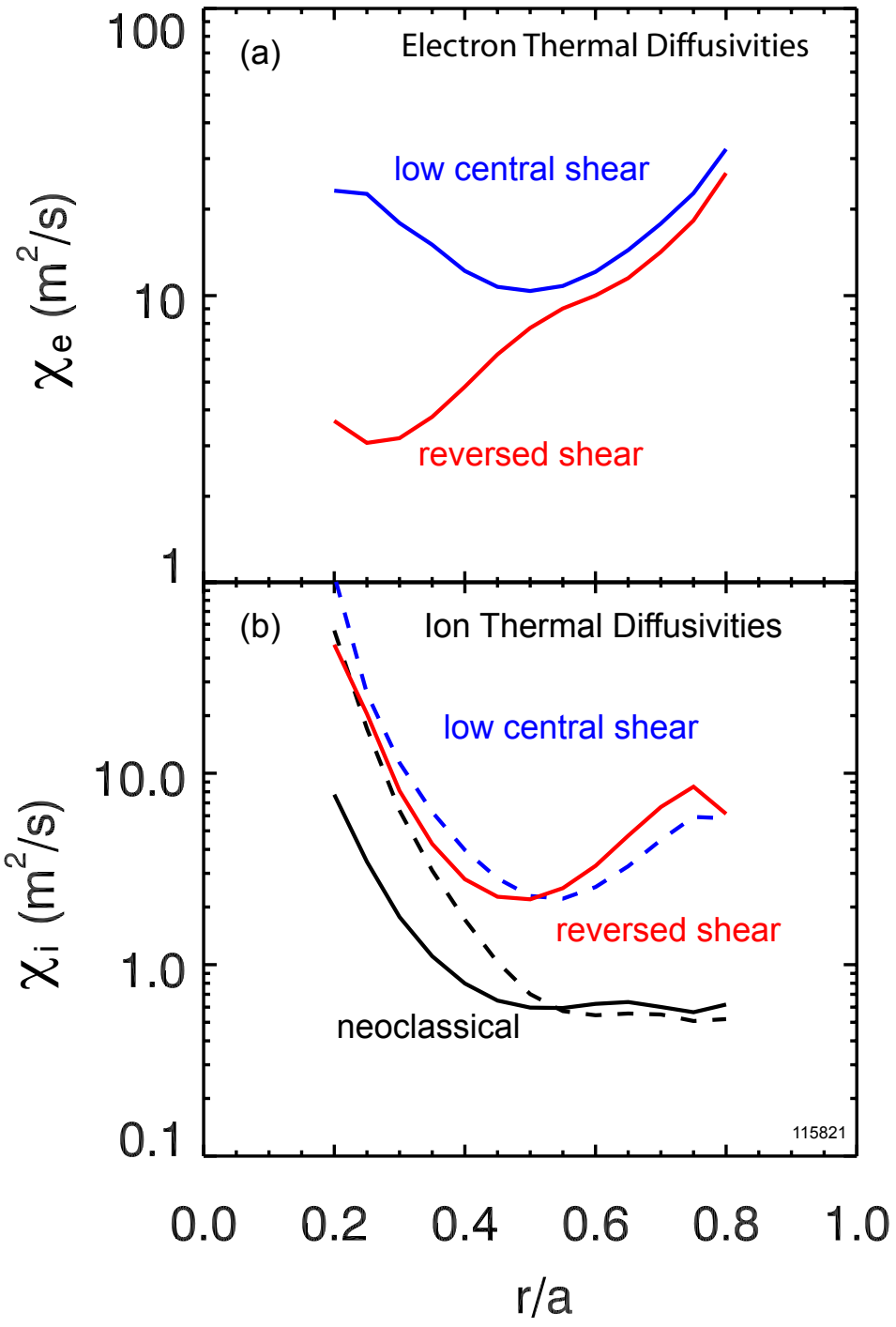

Figure 14: The (a) electron thermal diffusivity for the low central shear and reversed shear of the same discharge at different times. (b) Comparison of ion thermal diffusivity of the reversed shear (solid red), low central shear (dashed blue) and neoclassical calculations for low central shear (dashed black) and reversed shear (solid black).